remote sensing

MDPI

Article

Perspective of a Ku-Ka Dual-Frequency Scatterometer for Simultaneous Wide-Swath Ocean Surface Wind and Current Measurement

Yuanjing Miao [1,2], Xiaolong Dong [1,2,3,*], Qingliu Bao [4] and Di Zhu [1]

1 Key Laboratory of Microwave Remote Sensing, National Space Science Center, Chinese Academy of Sciences, Beijing 100190, China; Miaoyuanjing16@163.com (Y.M.); zhudi@mirslab.cn (D.Z.)
2 University of Chinese Academy of Sciences, Beijing 100049, China
3 International Space Science Institute-Bejing, Beijing 100190, China
4 Beijing Piesat Information Technology Co., Ltd., Beijing 100195, China; baoqingliu@piesat.cn
* Correspondence: dongxiaolong@mirslab.cn; Tel.: +86-10-6258-2841

Received: 2 May 2018; Accepted: 24 June 2018; Published: 02 July 2018

Abstract: Ocean surface wind and current are essential ocean dynamic environment and climate variables, and simultaneous observations at high resolution have attracted considerable interest. The study on surface wind and current will improve our knowledge of energy transfer between the atmosphere and the ocean, as well as the advection of heat, nutrients, and pollutants in the ocean. Since ocean surface wind and current are tightly coupled, we discuss the wind speed and direction errors effects on current, and find that current velocity is sensitive to wind speed and direction errors. Thus, it is necessary to obtain simultaneous wind field information to mitigate the effects of the wind on current retrieval. In this study, we present a Ka-Ku dual-frequency pencil-beam Doppler Scatterometer (DopScat), keeping the Ku-band for wind measurement and the Ka-band for current measurement. We establish an end-to-end simulation model to analyze the performance of the dual-frequency DopScat, and discuss the effects of satellite attitude and velocity determinations on current retrieval. The system parameters were optimized based on the simulation model. The simulation results show that the K_{pc} of the Ku-band DopScat is better than that of the traditional fan-beam and pencil-beam scatterometer, which is beneficial to improve wind measurement accuracy. In the Ka-band DopScat, the standard deviations (Stds) of current velocity in both along-track and cross-track directions could be smaller than 0.05 m/s, when the wind speed is larger than 5 m/s. When the wind speed is 7 m/s, the current field effective swath is 660 km, accounting for 63% of the DopScat swath, with an accuracy of 0.05 m/s. Our results indicate that the use of a Ku-Ka dual-frequency DopScat could be a feasible method for wide-swath and high-accuracy simultaneous measurements of ocean surface wind and current.

Keywords: ocean surface current; surface wind; dual-frequency; DopScat; end-to-end; wide-swath; high-accuracy

1. Introduction

Ocean surface wind and current are tightly coupled surface environment parameters. Surface wind drives current, but in turn, it is modulated by current because the forcing wind stress is pertinent to the current's moving reference frame [1]. In addition, surface wind affects current by changing the small-scale geometry of the ocean surface [2]. Ocean surface wind and current influence the exchanges of gases, heat, moisture, energy, and momentum between the atmosphere and the ocean. The measurements of oceanic quantities and atmosphere-ocean interaction processes play a key role in weather and ocean state forecasting, as well as in oceanography and climate research. For these

reasons, it is desirable to be able to obtain simultaneous synoptic measurements of ocean surface current and wind on a global scale.

In early ocean surface current studies, in situ measurement was a common and traditional method. The electromagnetic current meter is a sensor used for in situ measurement, and the measurement accuracy could be as small as 1 cm/s [3]. The acoustic Doppler current profiler (ADCP) is another sensor for in situ measurement which measures the Doppler frequency of sound in the water, and its measurement accuracy is better than 10% [4]. High-frequency (HF) ground-wave radar is a remote sensing method for ocean surface current measurement (i.e., The Ocean State Monitor and Analysis Radar (OSMAR 2003)), and the Std of current velocity is around 13 cm/s [5]. A common feature of in situ measurement and HF ground-wave radar is that they both could have high accuracy, but only in local offshore areas, which cannot meet the global coverage requirement.

At present, the global ocean current is measured by spaceborne altimeter and synthetic aperture radar (SAR). The geostrophic current can be retrieved from the precise altitude difference of ocean surface measured by a spaceborne altimeter [6]. However, an altimeter could only offer the macroscale circulation of the ocean surface. As for spaceborne SAR, which uses the Doppler centroid anomaly and along-track interferometry technique [7], it can achieve a world-wide observation, albeit at a lower resolution and accuracy [8]. In the last few years, the potential of scatterometer instruments for simultaneous ocean vector wind and surface current retrievals has gained great interest [9,10]. Rodriguez et al. [11,12] suggested that a slight modification of the pencil-beam scatterometer to include Doppler measurements could produce wide-swath vector surface current measurements. Fois et al. [13,14] showed that the Doppler shift could be estimated from a combination of two linear frequency modulated pulses: one with increasing frequency in time, i.e., up-chirp, and the other with decreasing frequency, i.e., down-chirp. Bao et al. [15] analyzed the feasibility of current measurement using a pencil-beam scatterometer.

The Doppler Scatterometer (DopScat) is a new type of marine remote sensing radar that maintains the ocean vector wind capability but also extends to Doppler shift estimation capability with sufficient accuracy for surface current estimation, by measuring the interferometric phase differences between pulses. Ocean surface current is estimated with Doppler measurements, and ocean surface wind measurement has a heritage with a pencil-beam scatterometer. So far, there is no dual-frequency DopScat operating in orbit.

In this paper, we present a Ku-Ka dual-frequency DopScat for wide-swath and high-accuracy simultaneous measurements of ocean surface wind and current. Considering that the Ka-band DopScat has a better performance in both effective wide-swath and high-accuracy, the ocean surface Doppler frequency and moving velocity measurement are mainly implemented by the Ka-band. In the ocean environment, ocean surface wind, wave, and current are tightly coupled. Moreover, wind and wave could have a significant impact on current retrieval, by affecting the Doppler model. In the upwind direction, for the case of receiving and transmitting in horizontal polarization (HH polarization), the current velocity error could be as large as 0.30 m/s for a wind speed error of 2 m/s, while in the case of receiving and transmitting in vertical polarization (VV polarization), the current velocity error could be as large as 0.20 m/s for a wind speed error of 2 m/s. In order to accurately measure the ocean surface current, it is necessary to obtain simultaneous wind field information to mitigate the effects of the wind and wave on current measurement. The simultaneous wind measurement is implemented by the Ku-band, and provides an auxiliary method in current measurement. In China, the planning of the CFOSAT (China-France Oceanography Satellite, which will be launched in October 2018) follow-on is currently underway. It is being considered that a new wave-current-wind series will be developed based on the CFOSAT wave-and-wind simultaneous observation capability. The research in this paper aims to provide support for the CFOSAT follow-on scatterometer system.

The dual-frequency Doppler scatterometer (DfDopScat) concept and measurement principle are presented in Section 2. The DfDopScat system simulation and performance analysis are presented in Section 3. The effects of satellite attitude and velocity determinations on current velocity retrieval are presented in Section 4. Conclusions are provided in Section 5.

2. Theory

2.1. The Need for Wind Measurement

Ocean surface wind and current are tightly coupled, and wind has a significance effect on current retrieval by affecting the Doppler spectrum model. In this paper, we propose a Ku-Ka dual frequency scatterometer for simultaneous ocean surface wind and current measurement, keeping the Ku-band for wind measurement to mitigate the effects of wind on current.

The frequency of radar echoes, backscattered by a moving target, experience a Doppler shift that is proportional to the target's line-of-sight velocity. The Doppler frequency of the radar backscatter from a moving target can be given by [16]:

$$f_D = -\frac{k_e}{\pi} \cdot V_r. \tag{1}$$

Here, k_e is the magnitude of the electromagnetic wave vector and V_r is the radial velocity component of the target. In our convention, a positive value of V_r corresponds to a negative Doppler frequency for a target, which is away from the radar.

At the ocean surface, for moderate incidence angles, the microwave backscattering is dominated by resonant Bragg scattering. Some Doppler shift would result from the phase velocity of the Bragg waves. If there is no surface current nor long waves, the Doppler spectrum would consist of two lines corresponding to the Bragg wave components velocity, which would travel toward and away from the radar. If surface current is present, both lines would experience an additional frequency shift in the same direction. If no surface current is present, the zeroth-order Doppler frequency would be caused by the Bragg wave phase velocity. This can be written as:

$$f_{D_\pm}^0 = \mp\frac{1}{2\pi}\left\{gk_B\left[1+\left(\frac{k_B}{k_0}\right)^2\right]\right\}^{0.5}, \tag{2}$$

where the subscripts + and − denote the two Bragg wave components travelling toward and away from the radar, g is the acceleration due to gravity, k_B is the magnitude of the Bragg wave vector, and $k_B = 2sin\theta \cdot k_e$, $k_0 = 363$ rad/m. If surface current is present, the zeroth-order Doppler frequency would be caused by the Bragg wave phase velocity and surface current, and can be written as:

$$f_{D_\pm}^0 = \mp\frac{1}{2\pi}\left\{gk_B\left[1+\left(\frac{k_B}{k_0}\right)^2\right]\right\}^{0.5} + \frac{1}{2\pi}\vec{k_B}\cdot\vec{V}. \tag{3}$$

Here, $\vec{k_B}$ is the Bragg wavenumber vector and $\vec{V}$ is the current velocity vector.

The ocean surface Doppler spectrum is considered as the distribution of Doppler frequencies associated with standardized small backscattered elements. For a single sinusoidal wave, the first moments of the two Bragg wave components distributions are:

$$\langle f_{D_\pm}\rangle_\sigma = f_{D_\pm}^0 + \frac{1}{2}Re\{D^*M_{1\pm}\}k^2\zeta^*\zeta, \tag{4}$$

where the symbol $\langle\ \rangle$ is the expectation operator, the subscript σ of $\langle f_{D_\pm}\rangle_\sigma$ indicates that this expectation value characterizes the mean value of the normalized radar cross section (NRCS), the NRCS of the ocean surface is relevant to the wind speed and direction, D is the complex Doppler modulation transfer function (MTF), $M_{1\pm}$ is a linear MTF describing the relation between the first-order slope and oscillation, k is the wavenumber, and ζ is the surface elevation. The second-order moments are:

$$\langle f_{D_\pm}^2\rangle_\sigma = \left(f_{D_\pm}^0\right)^2 + f_{D_\pm}^0 Re\{D^*M_{1\pm}\}k^2\zeta^*\zeta + \frac{1}{2}D^*Dk^2\zeta^*\zeta + O\left(\zeta^4\right), \tag{5}$$

Neglecting the contributions beyond second-order, for a single sinusoidal wave, the variance can be expressed as:

$$\langle f_{D_\pm}^2 \rangle_\sigma - \langle f_{D_\pm} \rangle_\sigma{}^2 = \frac{1}{2} D^* D k^2 \zeta^* \zeta. \tag{6}$$

At the ocean surface, the waves consist of a serious of single sinusoid waves, replacing finite amplitudes in Equations (4) and (6) with differential amplitudes and integrating over the wave spectrum. Thus, the total Doppler spectrum parameters can be written as:

$$\langle f_{D_\pm} \rangle_\sigma = f_{D_\pm}^0 + Re\{\iint D^*(k) M_{1\pm}(k) k^2 \psi(k) d^2k\}. \tag{7}$$

We use γ^2 as a variance symbol in the following:

$$\gamma_{D_\pm}^2 = \langle f_{D_\pm}^2 \rangle_\sigma - \langle f_{D_\pm} \rangle_\sigma{}^2 = \iint D^*(k) M_{1\pm}(k) k^2 \psi(k) d^2k. \tag{8}$$

Here, ψ denotes the wave height spectrum, defined as:

$$\psi(k)\delta(k-k') = \frac{1}{2}\langle \hat{\zeta}^*(k')\hat{\zeta}(k) \rangle. \tag{9}$$

Using the mean value and variance given by Equations (7) and (8), and normalizing Doppler frequency with σ, we finally obtain the Doppler spectrum model:

$$S(f_D) = \frac{\langle \sigma_+ \rangle}{\sqrt{2\pi\gamma_{D_+}^2}} e^{(f_D - \langle f_{D_+} \rangle_\sigma)^2 / \gamma_{D_+}^2} \frac{\langle \sigma_- \rangle}{\sqrt{2\pi\gamma_{D_-}^2}} e^{(f_D - \langle f_{D_-} \rangle_\sigma)^2 / \gamma_{D_-}^2}. \tag{10}$$

Based on the composite surface model proposed by Romeiser [16,17], the ocean surface Doppler spectrum model can be expressed as in Equation (10). The Doppler spectrum input parameters include wind speed and direction. The wind speed and direction errors will cause surface Doppler shift errors, and finally lead to current velocity errors. In the simulation, we use the Apel spectrum [18] and cosine-shape directional distribution function [19] as the ocean wave model. In Sections 2.1.1 and 2.1.2, we discuss the influence of wind speed and direction errors on current retrieval.

2.1.1. Effects of Wind Speed Errors on Current Retrieval

In Figures 1 and 2, we show the simulated ocean surface Doppler shift errors at different wind speed errors in the downwind and upwind directions.

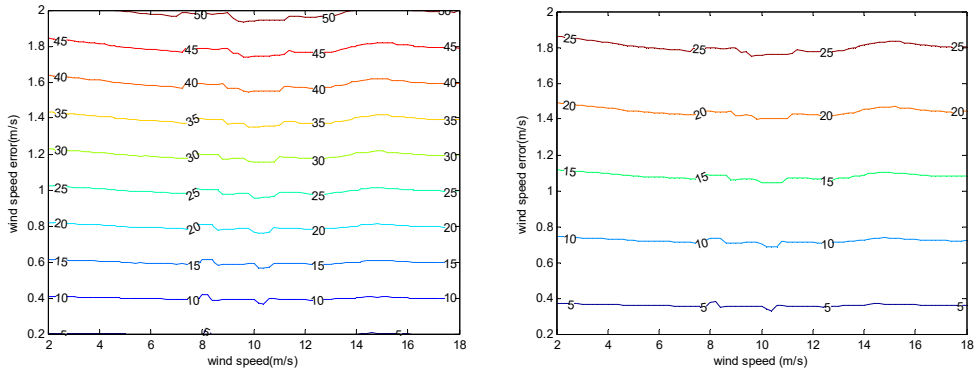

(**a**) (**b**)

Figure 1. Surface Doppler shift errors due to different wind speed errors in the downwind direction: (**a**) received and transmitted in horizontal polarization (HH polarization); (**b**) received and transmitted in vertical polarization (VV polarization).

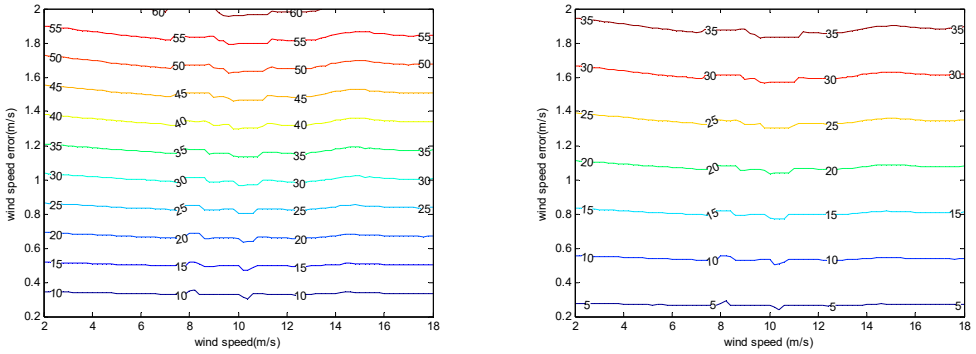

(**a**) (**b**)

Figure 2. Surface Doppler shift errors due to different wind speed errors in the upwind direction: (**a**) HH polarization; (**b**) VV polarization.

Based on these simulations (see Figures 1 and 2), as for Doppler shift errors due to wind speed errors, we found that HH polarization is very sensitive in both downwind and upwind directions. In the downwind direction, with a wind speed error of 2 m/s, the HH and VV polarization Doppler shift errors are around 50 Hz and 25 Hz, respectively. In the upwind direction, with a wind speed error of 2 m/s, the HH and VV polarization Doppler shift errors are around 60 Hz and 35 Hz, respectively.

In Figures 3 and 4, we show the simulated ocean surface current velocity errors due to different wind speed errors in the downwind and upwind directions, respectively.

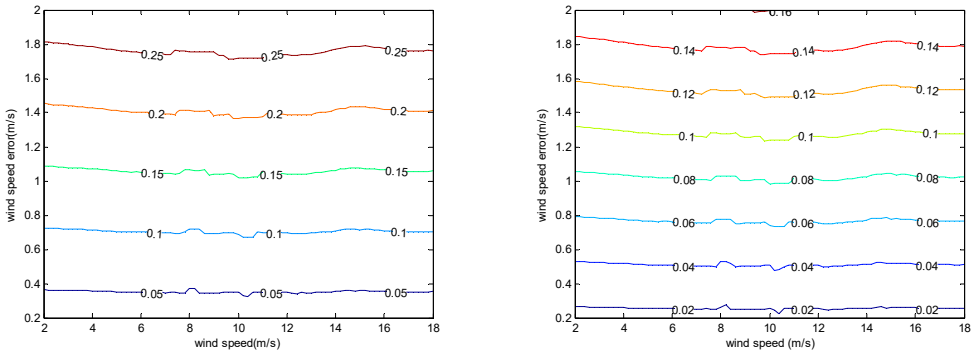

(**a**) (**b**)

Figure 3. Surface current velocity errors due to different wind speed errors in the downwind direction: (**a**) HH polarization; (**b**) VV polarization.

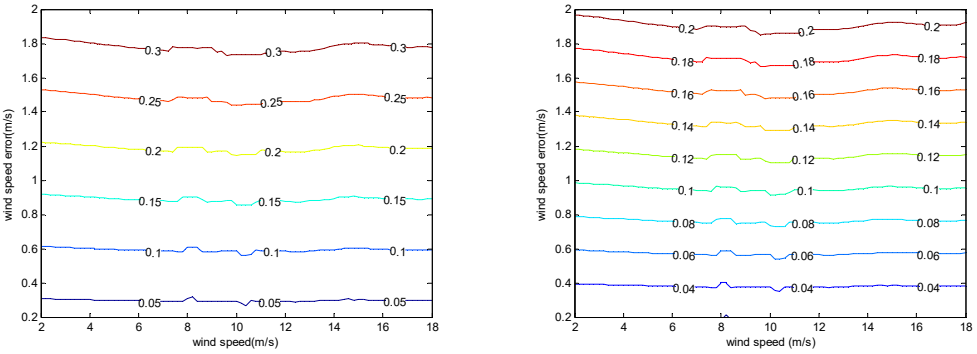

(**a**) (**b**)

Figure 4. Surface current velocity errors due to different wind speed errors in the upwind direction: (**a**) HH polarization; (**b**) VV polarization.

Based on these simulations (see Figures 3 and 4), as for surface current velocity errors due to wind speed errors, we found again that HH polarization is very sensitive in both the downwind and upwind directions. In the downwind direction, with a speed error of 2 m/s, the surface current velocity errors for HH and VV polarization are 0.25 m/s and 0.14 m/s, respectively. In the upwind direction, at a speed error of 2 m/s, the current velocity errors for HH and VV polarization are 0.30 m/s and 0.20 m/s, respectively.

2.1.2. Effects of Wind Direction Errors on Current Retrieval

In Figures 5 and 6, we show the simulated ocean surface current Doppler shift errors and current velocity errors due to different wind direction errors, respectively.

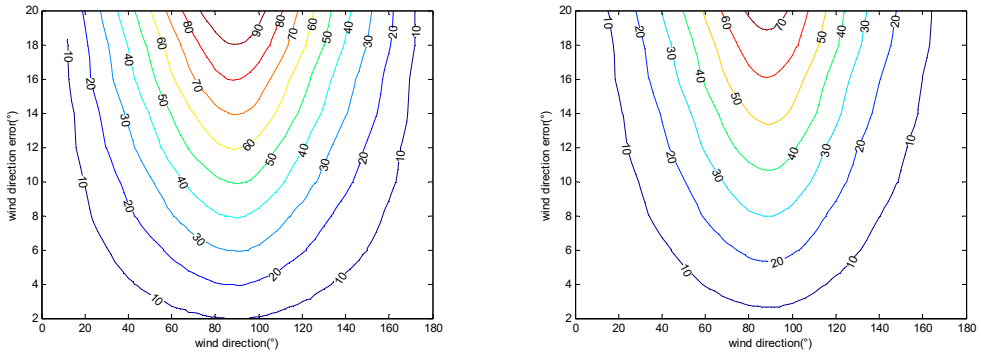

(**a**) (**b**)

Figure 5. Surface Doppler shift errors due to different wind direction errors: (**a**) HH polarization; (**b**) VV polarization.

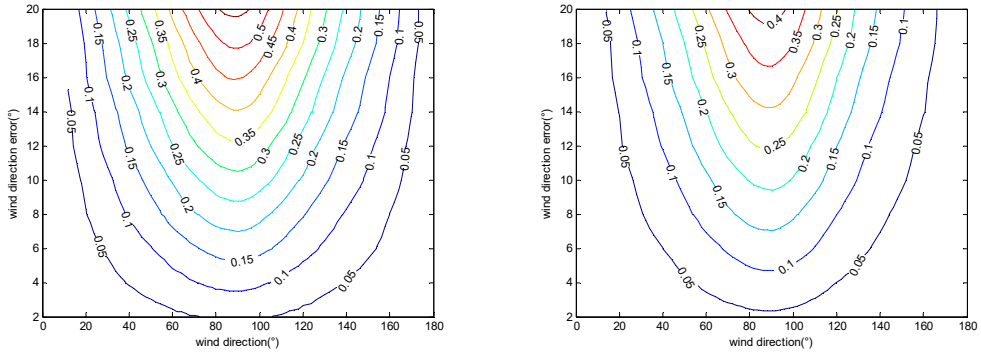

(**a**) (**b**)

Figure 6. Surface current velocity errors due to different wind direction errors: (**a**) HH polarization; (**b**) VV polarization.

As shown in Figure 5, the wind direction errors have an impact on the ocean surface Doppler shift, especially in the crosswind direction. In this direction, Doppler shift errors caused by wind direction errors for the HH polarization are 90 Hz, or 70 Hz for VV polarization. Figure 6 shows that, in the crosswind direction, the current velocity error is 0.50 m/s (around 0.40 m/s) when the wind direction error is 20° for HH polarizations (for VV polarization).

From the analyses above, we conclude that the wind speed and direction errors have significant effects on current velocity, mainly induced by affecting the ocean surface Doppler shift. The ocean surface current velocity errors are sensitive to the wind speed and direction errors. For HH polarization, the current velocity error could be as large as 0.25 m/s for a wind speed error of 2 m/s, while it reduces to even smaller than 0.50 m/s in case of a wind direction error that is smaller than 20° in the crosswind direction. In the case of VV polarization, the ocean surface current velocity error could be as large

as 0.14 m/s for a wind speed error of 2 m/s, and could reach values smaller than 0.40 m/s for wind direction errors smaller than 20° in the crosswind direction.

In addition, wind speed in the Ka-band will experience a saturation beginning at 15 m/s [20]. The Ka-band geophysical model function (GMF) indicates that the saturation is somewhere above 15–20 m/s, as the GMF follows the observation and the theoretical power law well, while the airborne results suggest that it will function better than the GMF theory [21], which may due to the deeper penetration of the airplane observations. Because wind has a significant effect on current, we propose a Ku-Ka dual-frequency scatterometer for simultaneous wind and current measurement.

2.2. Dual-Frequency Measurement

The Ku-band and the Ka-band simultaneously operate and sharing the same reflector antenna with separated feed horns. In order to reduce the loss due to scanning, separated transmitting and receiving feed horns for the Ka-band are considered. The scanning geometry of the DfDopScat is shown in Figure 7.

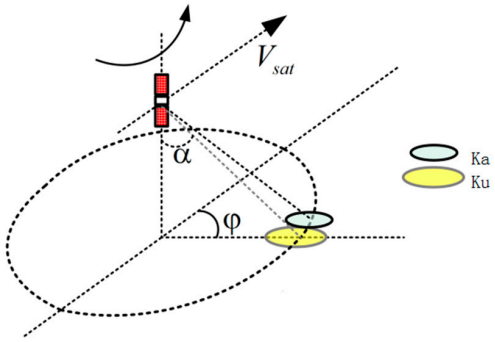

Figure 7. Dual-frequency Doppler scatterometer (DfDopScat) scanning geometry.

The reflector antenna is conically scanned. In a pencil-beam system, the reflector antenna is continuously rotated and the scanning motion causes the antenna footprint to sweep over the surface. The antenna footprint is defined as the antenna pattern two-way 3 dB contour projected on the Earth's surface.

The antenna's rotation is an important issue for a pencil-beam system to ensure the spatial continuity of the measurements. During the rotation of the antenna, the along-track continuity constraint means that the satellite does not move a distance larger than the elevation width of the footprint. This insures that adjacent measurements will be contiguous in elevation. The antenna spins at a rate of Ω per second, which can be summarized as:

$$\Omega \geq \frac{V_g}{x_{el}}. \tag{11}$$

Here V_g is the satellite velocity projected on the Earth's surface and x_{el} is the elevation width of the footprint.

2.3. Measurement Principle of DopScat Based On the Pencil-Beam System

The DopScat based on pencil-beam rotating observation geometry measures the Doppler shift of echoes by pulse interference [9], which exploits the technique of pulsed Doppler measurement. The interferometry measurement principle of DopScat is shown in Figure 8. When the time, t, is zero, the distance between the radar and the target is r; when the time, t, is τ, the distance is r. The distance difference of the target at these two moments is Δr, and the phase difference of the radar echoes at these two moments is $\Delta\phi$:

$$\Delta\phi = 2k\Delta r. \tag{12}$$

Here, k is the wavenumber of the electromagnetic wave. The radial velocity component can be written as:

$$V_r = \frac{\Delta r}{\tau} = \frac{\Delta \phi}{2k\tau}. \tag{13}$$

Through the radial velocity components V_{r1} and V_{r2}, observed at two different azimuths, we can estimate the velocity vector of the target. The observation geometry of the pencil-beam scatterometer is shown in Figure 9.

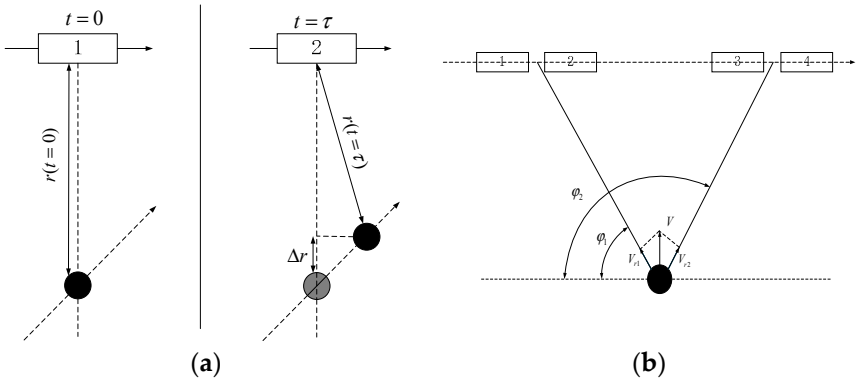

Figure 8. Measurement principle: (**a**) pulse pair phase difference; (**b**) current vectors are estimated by combining multiple (2–4) radial velocity measurements.

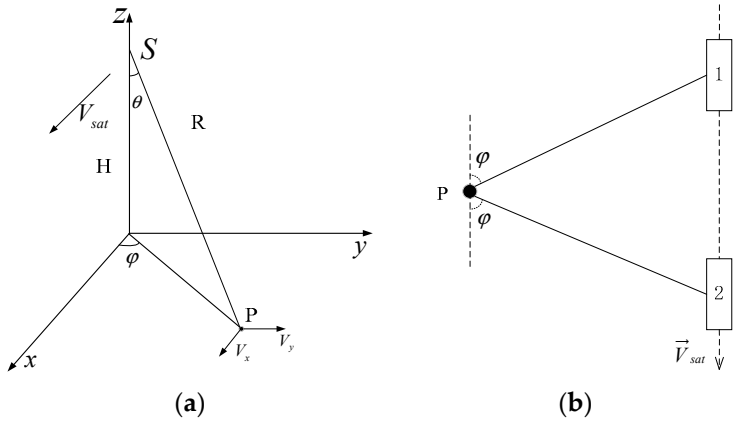

Figure 9. Observation geometry of the pencil beam rotating scatterometer: (**a**) three-dimensional view; (**b**) different azimuth angle relations.

According to the observation geometry, the Doppler shift can be expressed as follows:

$$f_d = \frac{2V_r}{\lambda} = \frac{2sin\theta\left[(V_{sat} - V_x)cos\varphi - V_y sin\varphi\right]}{\lambda}. \tag{14}$$

Here, V_r is the relative radial velocity, λ is the electromagnetic wave length, and V_{sat} is the satellite velocity. The target P could be observed at least in two observation azimuths, φ and $\pi - \varphi$. The time interval of the two successive echoes is τ, so the interferometric phases of the two successive echoes at two observation azimuths, φ and $\pi - \varphi$, can be described as follows:

$$\Phi_1 = \frac{4\pi sin\theta\left[(V_{sat} - V_x)cos\varphi - V_y sin\varphi\right]}{\lambda}\tau, \tag{15}$$

$$\Phi_2 = \frac{4\pi sin\theta\left[-(V_{sat} - V_x)cos\varphi - V_y sin\varphi\right]}{\lambda}\tau. \tag{16}$$

Here $\tau = 1/\text{PRF}$ (PRF stands for pulse repetition frequency). So, we can measure the target velocity vector by the interference phases of the two successive echoes observed at two different azimuths. Then, by solving Equations (15) and (16), we can obtain:

$$V_x = V_{sat} + \frac{\lambda}{8\pi sin\theta cos\varphi\tau}(\Phi_2 - \Phi_1), \tag{17}$$

$$V_y = -\frac{\lambda}{8\pi sin\theta sin\varphi\tau}(\Phi_2 + \Phi_1). \tag{18}$$

2.4. Pulse Sequence

The pulse sequence plays a crucial role in a radar system. A high PRF is required for the pulsed Doppler measurement, where the PRF needs to be larger than the Doppler bandwidth (i.e., $\text{PRF} \geq B_{doppler}$). The Doppler bandwidth varies with the observation azimuth and the antenna 3 dB azimuth beam width, as shown in Equation (19):

$$B_{doppler} = \frac{4V_{sat}sin\varphi sin\frac{\beta_{az}}{2}}{\lambda}. \tag{19}$$

Here, β_{az} is the antenna 3 dB azimuth beam width, for a given size antenna, and the 3 dB azimuth beam width is determined. In Figure 10, we show Doppler bandwidths in different observation azimuths with different antenna sizes.

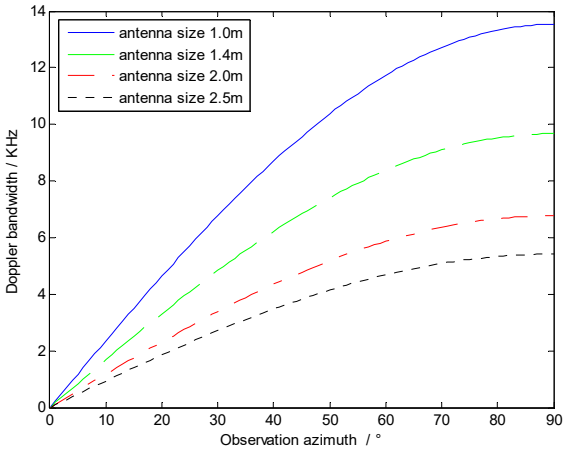

Figure 10. Doppler bandwidths in different observation azimuths with different antenna sizes.

The Doppler bandwidth varies as a function of the observation azimuth and antenna azimuth beam width. For a given antenna size, its azimuth beam width is also known. As shown in Figure 10, the Doppler bandwidths increase as the observation azimuths increase, reaching a maximum in the side-looking direction. To perform pulsed Doppler measurements, the PRF should be larger than the Doppler bandwidth. Assuming, as an example, a size of the antenna of 1.0 m, we obtain a Doppler bandwidth in the side-looking direction of 13.54 kHz. Thus, the PRF in this case should be larger than 13.54 kHz. For an antenna of 2.5 m, the corresponding PRF should be larger than 5.6 kHz. Considering the limited size of the satellite platform, the largest acceptable antenna size is 1.4 m for the proposed scatterometer system, and the PRF in this case should be larger than 9.5 kHz.

The PRF is also related to the spatial decorrelation, which can be written as [15]:

$$\gamma_{spatial} = \frac{\int \exp\left(-j\frac{4\pi}{\lambda}\cdot\frac{V_{sat}sin\theta cos\varphi}{PRF}\right)sinc\left(\frac{\varphi-\varphi_0}{R_\varphi}\right)^2 d\varphi}{\int sinc\left(\frac{\varphi-\varphi_0}{R_\varphi}\right)^2 d\varphi}. \tag{20}$$

The spatial decorrelation of the two successive echoes is formed due to the different observation geometries. The separation between the two observation geometries is called the baseline, $B_{baseline}$:

$$B_{baseline} = V_{sat} \cdot \tau = V_{sat} / \mathrm{PRF}. \quad (21)$$

Here, V_{sat} is the satellite velocity, and τ is the time interval of the two successive echoes $\tau = 1/PRF$. If the baseline $B_{baseline}$ is too short, the sensitivity to echo phase differences would be undetectable, while if the baseline $B_{baseline}$ is too long, additional noise due to spatial decorrelation corrupts the echo signals. In Equation (20), the spatial decorrelation is relevant to the baseline and the observation azimuths. For a given satellite platform height, the satellite velocity is determined; therefore, the baseline $B_{baseline}$ is mainly affected by the PRF. More specifically, the spatial decorrelation is determined by the PRF and the observation azimuth. The relationship between the PRF and spatial decorrelation in different observation azimuths is presented in Figure 11.

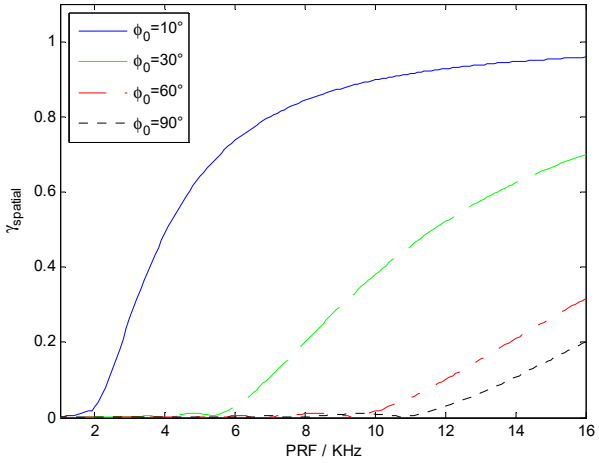

Figure 11. The relationship between the pulse repetition frequency (PRF) and spatial decorrelation in different observation azimuths.

As shown in Figure 11, the spatial decorrelation coefficient decreases at a higher value of the observation azimuth. When the PRF is smaller than the Doppler bandwidth $B_{doppler}$, the spatial decorrelation coefficient tends to be zero, i.e., the two successive echoes are uncorrelated. As for the spatial decorrelation term, it also requires that PRF $\geq B_{doppler}$.

To achieve a high PRF, a modified pulse sequence is required, as shown in Figure 12. The modified pulse sequence [15] is applied in the following system simulation.

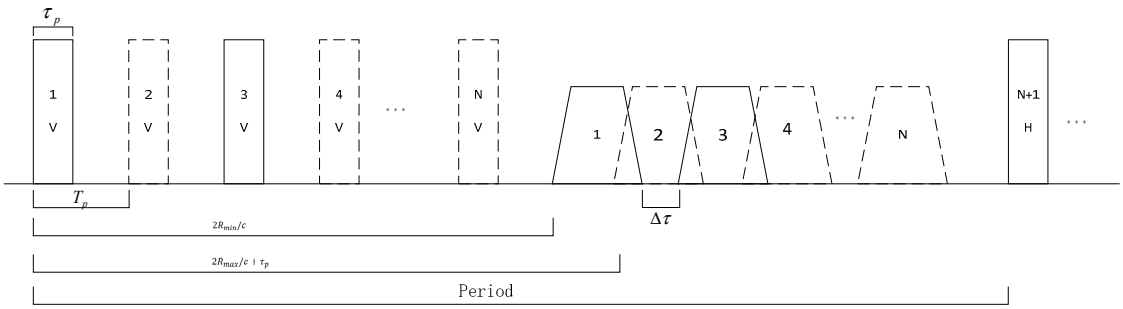

Figure 12. The modified pulse sequence.

Figure 12 shows the modified pulse sequence. Rectangles represent the transmit pulse, trapezoids represent return echoes, R_{max} and R_{min} denote the farthest and nearest slant distance from the radar

to the footprint, respectively, 'V' and 'H' denote V and H polarization, respectively, τ_p denotes the pulse length, T_p denotes the pulse repletion interval, Period denotes the burst repletion interval, and $\Delta\tau$ denotes the echo time offset in the receiving window. V polarization and H polarization are alternately transmitted.

2.5. Signal Processing

To minimize the limitations of range ambiguity, a pulse with different central frequency (i.e., the solid and dashed rectangles), $f_{\pm} = f_0 \pm \Delta f$, is transmitted on alternate pulses:

$$f_{\pm} = f_0 \pm \Delta f. \tag{22}$$

Here, f_0 is the carrier frequency and Δf is the frequency offset. To avoid the overlap of the echoes in frequency and ensure that they are separated in the receiving chain, one must ensure that:

$$2\Delta f \geq B. \tag{23}$$

Here, B is the bandwidth after full de-chirp operation. In the Ku-band DopScat, the bandwidth after the full de-chirp operation is 5.86 MHz, so the frequency offset has to be larger than 4.28 MHz. In the Ka-band DopScat, the bandwidth after the full de-chirp operation is 11.10 MHz, so the frequency offset has to be larger than 5.55 MHz.

The two types echoes (i.e., the solid and dashed trapezoidal), can be separated in frequency by signal processing in the receiver. The specific signal processing diagram is shown in Figure 13.

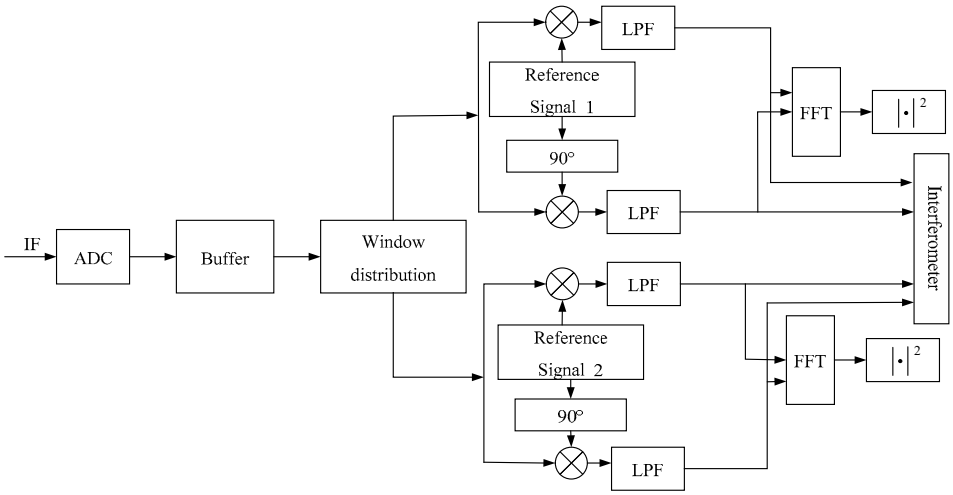

Figure 13. Diagram of signal processing.

The echo signal is directed to the receiver where it is amplified, down-converted, and detected. In a radar system, before the received signal is processed, the receiver converts the radio frequency signal (RF signal) into the intermediate frequency signal (IF signal). The IF signal is then in the buffer for processing after sampling by analog-to-digital (A/D). In order to separate the two successive types of echoes with different carrier frequencies, (i.e., the solid and dashed trapezoids), we can use two different reference signals (i.e., Reference signal 1 and Reference signal 2) with the same frequency as echo signals. The echoes and reference signals are used for pulse compression carried out by the full de-chirp operation, then the low-pass filter separates the echo signals. The two separated successive echo signals are employed for interferometry processing. The distance information can be obtained from the Fourier transform processing of the echo signals after the full de-chirp operation, providing the amplitude of the echo signals.

3. System Simulation

In the system simulation, we establish an end-to-end system simulation model, seen in Figure 14.

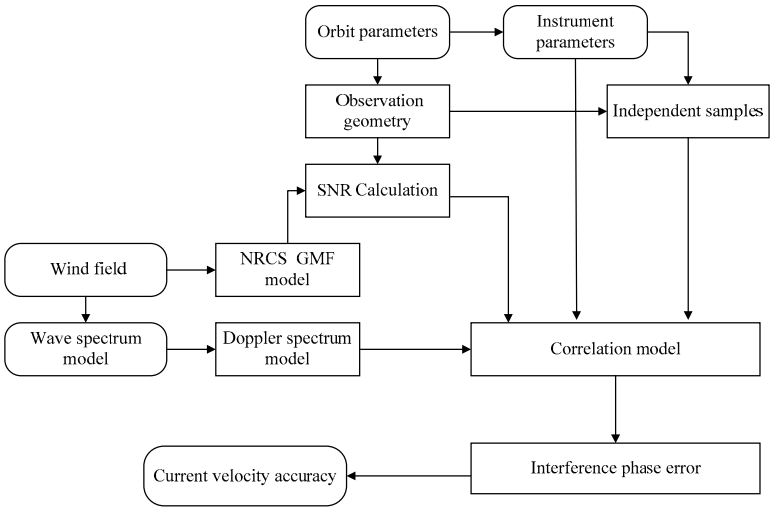

Figure 14. End-to-end system simulation model diagram.

In Figure 14, the inputs of the end-to-end simulation system model include orbital parameters, instruments parameters, ocean surface wind field, and the correlation model. The outputs are current velocity accuracies in the along-track and cross-track directions. For the correlation model, the complex correlation coefficient can be written as the products of four decorrelation terms [15]:

$$\gamma = \gamma_{thermal} \cdot \gamma_{footprint} \cdot \gamma_{spatial} \cdot \gamma_{temporal} \cdot \quad (24)$$

Here, γ is the complex correlation coefficient, $\gamma_{thermal}$ is the thermal decorrelation, $\gamma_{footprint}$ is the different observation regions decorrelation, $\gamma_{spatial}$ is the spatial decorrelation, and $\gamma_{temporal}$ is the temporal decorrelation.

In the simulation model, we chose the Apel spectrum [18] as the ocean wave spectrum model and cosine-shape function [19] as the ocean directional distribution function. We also used the composite surface Doppler spectrum model based on the simple equations of Bragg scattering theory proposed by Romeiser [16,17]. As for the NRCS GMF model, we used the NSCAT-2 model [22] in the Ku-band DopScat with an incident angle range of 16–66°, a wind speed range of 0.2–50 m/s, and a wind direction of 0–180°. The orbital parameters are listed in Table 1.

Table 1. Orbital parameters.

Earth Model	WGS-84
Orbit Height	520 km
Eccentricity	0
Orbit inclination	97.45°
Satellite Velocity	7606 m/s

3.1. Ku-Band System Simulation

3.1.1. System Parameters

The system parameters are listed in Table 2, but the PRF and bandwidth are not given. In order to better measure the Doppler shift, the system parameters should be optimized, especially the PRF and bandwidth. In the simulation, the orbital parameters are shown in Table 1.

Table 2. Main parameters of the Ku-band DopScat.

Parameters	Value
Transmitted Power	200 W
Carrier Frequency	13.256 GHz
Carrier Wavelength	2.26 cm
3dB Azimuth Beamwidth	0.96°
3dB Range Beamwidth	0.96°
Antenna Incidence Angle	48°
Antenna Gain	46 dB
Rotation Rate	18.3 rpm
System Loss	5 dB
System Temperature	290 K

3.1.2. PRF Optimization

The PRF determines the maximum pulse length and duty cycle, which are directly related to the signal-to-noise ratio (SNR). The higher the PRF is, the smaller the pulse length becomes. Based on the radar equation, a smaller pulse length produces a lower SNR, and gives rise to a smaller thermal noise decorrelation. However, a lower PRF means a longer interference time interval (as $\tau = 1/\mathrm{PRF}$, where τ is the interference time interval) and would give rise to a smaller spatial decorrelation [15,23]. Therefore, the choice of the PRF must be optimized. In the simulation, we chose the wind speed of 7 m/s (global average wind speed) and the wind direction of 90°. The wind direction has a modulation effect on the ocean surface backscattering coefficient, with the upwind direction presenting the largest backscattering coefficient, followed by the downwind direction and finally the crosswind direction. In our simulation, a wind direction of 90° was equivalent to the crosswind direction. Using another different direction would result in a better system performance and a smaller standard deviation. In order to scientifically justify the parameter optimization, we fixed the wind direction at 90°. We simulated surface current velocity components Std in the along-track and cross-track directions under these conditions, where the spatial resolution was 25 km × 25 km and the temporal resolution was 10 days. The results are shown inFigure 15, where the ordinates are the half of the swath and can be mirrored. In the figures below about the current field effective swath, the ordinates show the half of the swath and can be mirrored. If not otherwise specified, we adopted in our simulations a spatial resolution of 25 km × 25 km and a temporal resolution of 10 days.

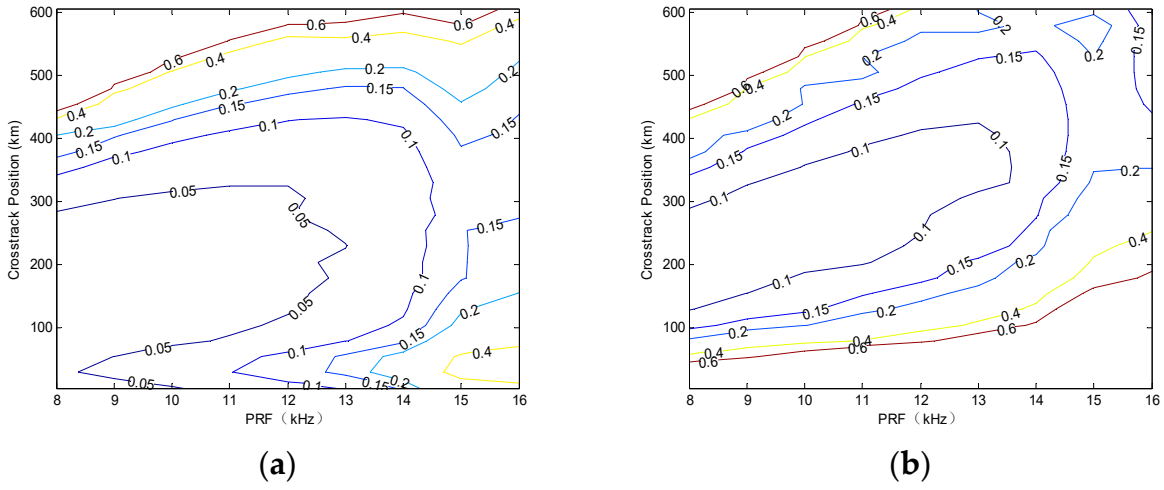

Figure 15. Current velocity components Std with PRF for a wind speed of 7 m/s and a wind direction of 90°: (**a**) along-track direction; (**b**) cross-track direction.

The current field effective swaths of different current velocity Stds are shown in Table 3. In the tables below about the current field effective swath, the effective swaths consider the whole swaths, not the half. When the current velocity Std reaches 0.10 m/s, the current field effective swath is defined as the cross-track distance, while current velocity Stds are smaller than 0.10 m/s in the both the along-track and cross-track directions.

Table 3. Current field effective swaths of different current velocity Stds with different values of PRF.

PRF (kHz)/Current Velocity Std (m/s)	8.0	9.0	10.0	11.0	12.0	13.0	14.0	15.0
0.10	326	342	358	378	328	220	-	-
0.15	488	538	606	604	596	544	414	-
0.20	574	632	696	704	708	686	594	220
0.25	668	726	780	766	768	770	704	436
0.30	696	766	816	814	894	828	770	512

In Table 3, for different current velocity Stds with different values of PRF, the current field effective swaths are different. For example, when the current velocity Std reaches 0.10 m/s, for a PRF of 10 kHz, the current field effective swath is 358 km, while for a PRF of 11 kHz it is around 378 km.

We consider here the trade-off between the current velocity Std and the current field effective swath. To optimize the PRF in the simulation, we chose 0.15 m/s as the current velocity Std. The current field effective swaths with different values of PRF, for a current velocity Std of 0.15 m/s, are listed in Table 4. Duty cycle here is defined as the ratio of the transmit signal duration with the whole duration of the transmitting and receiving signal in a pulse train.

Table 4. Current field effective swaths (current velocity Std of 0.15m/s) with different values of PRF.

PRF (kHz)	Duty Cycle	Current Field Effective Swath (km)
8.0	24.42%	488
9.0	21.22%	538
10.0	18.03%	606
11.0	14.83%	604
12.0	11.63%	596
13.0	8.43%	544
14.0	5.24%	414
15.0	2.04%	-

As shown in Table 4, the current field effective swath increases as the PRF increases, and it reaches a maximum of 606 km when the PRF is 10 kHz. If the PRF is greater or less than 10 kHz, the current field effective swath decreases. Finally, we chose 10 kHz as the optimized PRF.

3.1.3. Bandwidth Optimization

The bandwidth determines the range resolution of a radar system; a bigger bandwidth produces a higher range resolution, as well as more independent samples. However, the system noise power also increases with a larger bandwidth, which results in the decrease of the SNR. Thus, a trade-off exists between the bandwidth and SNR. When the wind speed is 7 m/s and the wind direction is 90°, the SNR with different bandwidths is shown in Table 5. We simulated the surface current velocity components Std in the along-track and cross-track directions; the results are shown in Figure 16. The current field effective swaths (current velocity Std of 0.15 m/s) with different bandwidths are presented in Table 6.

Table 5. Signal-to-noise ratio (SNR) with different bandwidths.

Bandwidth (MHz)	SNR_VV (dB)
1.0	10.14
1.5	8.38
2.0	7.13
2.5	6.16
3.0	5.37
3.5	4.70
4.0	4.13
4.5	3.61
5.0	3.15

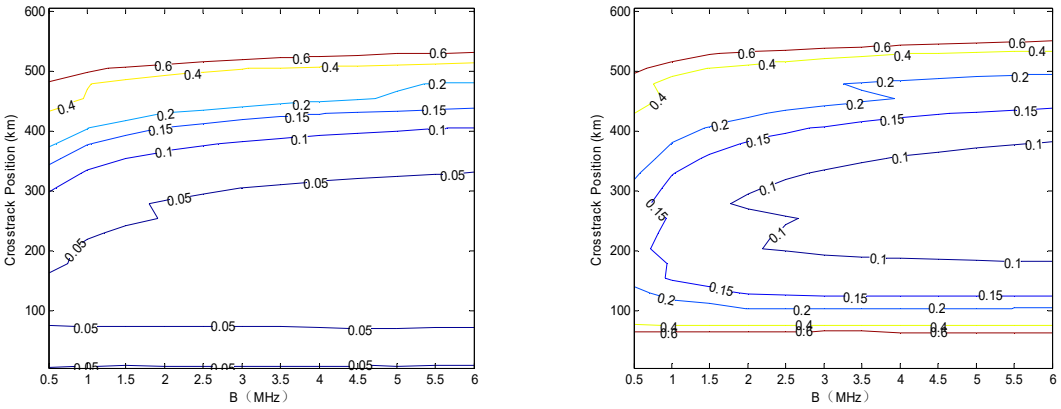

Figure 16. Surface current velocity components Std with bandwidths for a wind speed of 7 m/s and a wind direction of 90°: (**a**) along-track direction; (**b**) cross-track direction.

Table 6. Current field effective swaths (current velocity Std of 0.15 m/s) with different bandwidths.

Bandwidth (MHz)	Current Field Effective Swath (km)
1.0	352
1.5	442
2.0	510
2.5	544
3.0	561
3.5	580
4.0	596
4.5	600
5.0	609

As shown in Figure 16, the current field effective swath increases as the bandwidth increases. When the bandwidth is 5 MHz, the current field effective swath is largest, as shown in Table 6. However, a larger bandwidth produces a lower SNR, as presented in Table 5. In the correlation model, the SNR is related to the thermal decorrelation, and the thermal decorrelation requires a high SNR. Considering the trade-off between the SNR and current field effective swath, we chose 4 MHz as the optimized bandwidth.

3.1.4. System Performance

We simulated the system performance based on the system parameters (see Tables 1 and 2) for different wind speed conditions, where the wind speed varied from 2 to 21 m/s and wind direction

was 90°. Without loss of generality, the wind speed range includes low wind speed, moderate wind speed, and high wind speed in our simulations. The surface current velocity components Std under these conditions are shown in Figure 17, where σ_V, σ_{Vy}, and σ_{Vx} denote the line-of-sight direction, the cross-track direction, and the along-track direction, respectively.

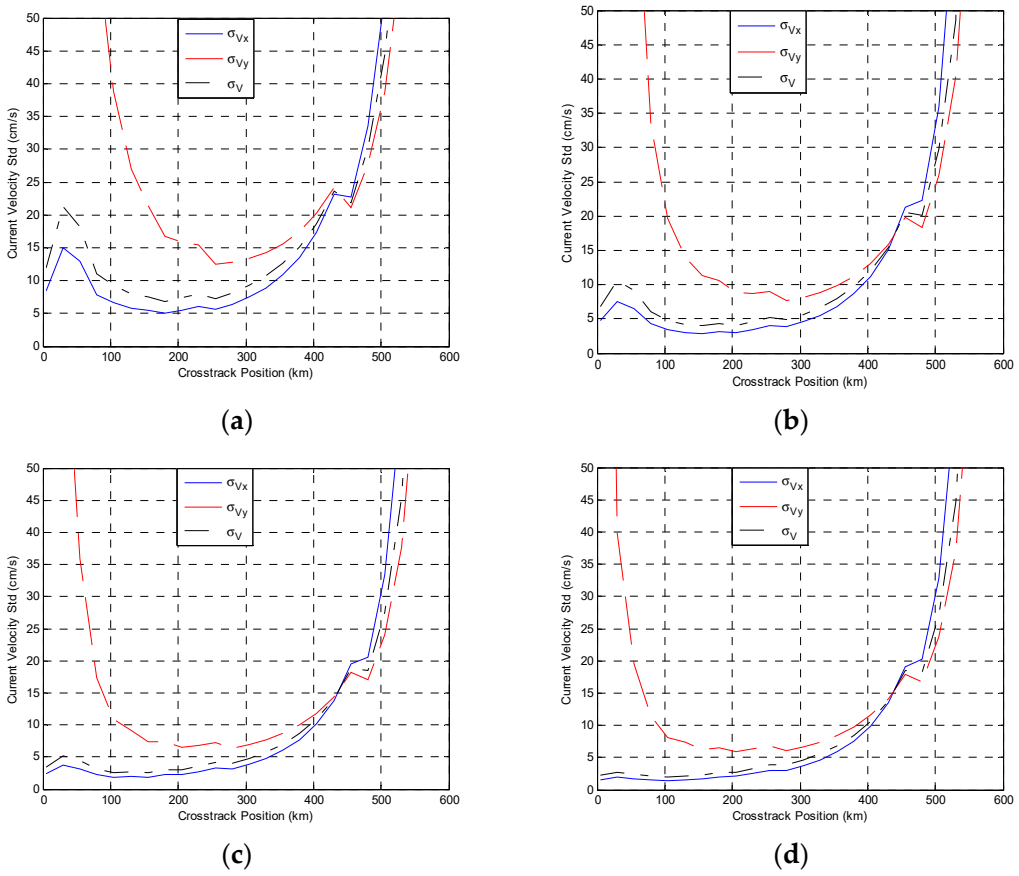

Figure 17. Surface current velocity components Std in line-of-sight, cross-track, and along-track directions with a wind direction of 90°: (**a**) U = 4 m/s; (**b**) U = 7 m/s; (**c**) U = 14 m/s; (**d**) U = 21 m/s.

As shown in Figure 17, we found that the current field effective swath is small in the condition of low wind speed, but has a good performance in the condition of high wind speed. In order to analyze the current field effective swaths of different current velocity Stds in different wind speeds more directly, we examined Table 7. From Table 7, we found that the current field effective swath (current velocity Std of 0.10 m/s) is zero when the wind speed is smaller than 6 m/s. When the wind speed is 7 m/s, the current field effective swath (current velocity Std of 0.10 m/s) is only around 270 km, accounting for 27.3% of the scatterometer swath (the swath is 1245 km). When the wind speed is 7 m/s, the current field effective swath (current velocity Std of 0.15 m/s) is 594 km.

Table 7. Current field effective swaths of different current velocity Stds in different wind speeds.

Wind Speed (m/s)/Current Velocity Std (m/s)	2	3	4	5	6	7	8	9	10	11	15	18	21
0.10	-	-	-	-	270	340	420	460	496	514	554	574	584
0.15	-	-	222	460	548	594	624	652	664	678	714	720	734
0.20	-	158	478	610	658	692	708	726	750	770	802	818	842
0.25	-	468	642	676	762	780	796	814	824	830	856	870	882
0.30	-	560	698	764	796	816	834	842	854	862	892	902	914

From the above analyses, in the Ku-band DopScat, the best achievable current velocity Std is 0.10 m/s but with small current field effective swath. So, in order to have a high-accuracy and wide-swath ocean current measurement, we propose a Ka-band DopScat.

3.1.5. Random Error K_{pc}

Random Error K_{pc} suggests the backscattering coefficient accuracy in a radar system. A smaller K_{pc} produces a higher backscattering coefficient accuracy. The accuracy of the backscattering coefficient has a significant effect on wind retrieval: a higher backscattering coefficient accuracy means a higher wind speed accuracy. Thus, a smaller value of K_{pc} means a higher wind speed accuracy. The K_{pc} can be expressed as:

$$K_{pc} = \sqrt{\left(A + \frac{B}{SNR} + \frac{C}{SNR^2}\right)}. \quad (25)$$

Here, the coefficients A, B, and C are related to the correlation statistics associated with a particular instrument, transmission modulation, and processor implementation [23,24].

We calculated the K_{pc} of the Ku-band DopScat and compared it with a traditional fan-beam scatterometer and a traditional pencil-beam scatterometer. Here, the traditional fan-beam and pencil-beam scatterometer refer to the CFOSAT scatterometer and the HY-2A scatterometer, respectively. The results are shown Figure 18, in which the spatial resolution of wind cell vector is 25 km × 25 km.

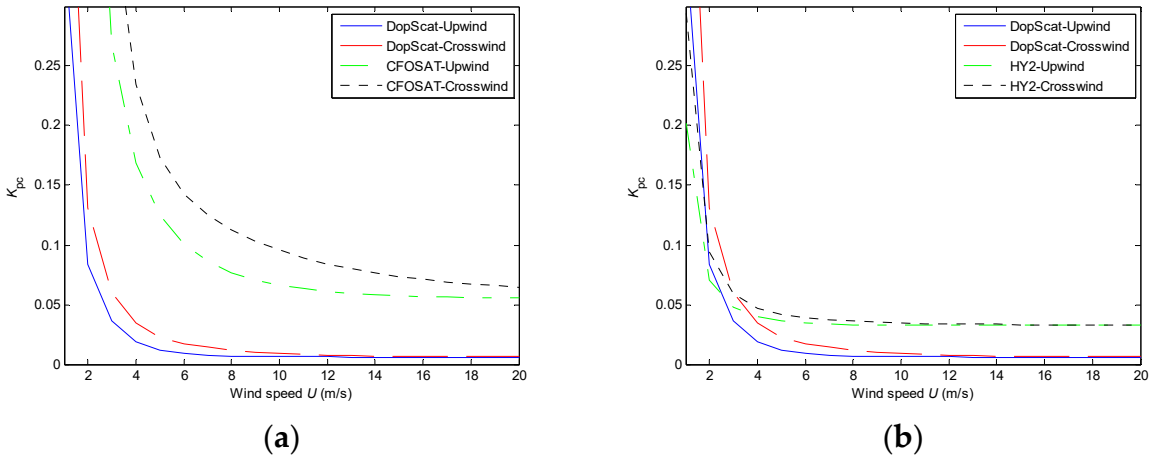

Figure 18. The value of K_{pc} with different wind speeds: (**a**) comparison of K_{pc} between DopScat and a traditional fan-beam scatterometer; (**b**) comparison of K_{pc} between DopScat and a traditional pencil-beam scatterometer.

We found that the K_{pc} of the Ku-band DopScat is always smaller than that of the CFOSAT scatterometer at any wind speed, as seen in Figure 16a. In Figure 16b, compared with the HY-2A scatterometer, the K_{pc} of the Ku-band DopScat is always better than that of the HY-2A scatterometer, except when the wind speed is less than 3 m/s. The Ku-band DopScat, even in a low wind speed, could still achieve a higher accuracy for the ocean surface backscatter coefficient. For example, when the wind speed is 4 m/s, the K_{pc} of the Ku-band DopScat is around 0.03, the K_{pc} of the CFOSAT scatterometer is 0.23—which is approximately 6 times larger than that of the Ku-band DopScat, and the K_{pc} of the HY-2A scatterometer is 0.05.

The above analysis indicates that in the Ku-band DopScat, the wind speed and direction accuracies are better than those of the HY-2A scatterometer, as the K_{pc} is smaller than that of the HY-2A scatterometer. For the HY-2A scatterometer, the wind speed accuracy is 2 m/s and the wind direction accuracy is within 20°.

3.2. Ka-Band System Simulation

3.2.1. System Parameter

Based on the end-to-end system simulation model, as presented in Figure 13, the main parameters of the Ka-band DopScat are listed in Table 8.

Table 8. Main parameters of the Ka-band DopScat.

Parameters	Value
Transmitted Power	150 W
Carrier Frequency	35.75 GHz
Carrier Wavelength	0.84 cm
3dB Azimuth Beamwidth	0.42°
3dB Range Beamwidth	0.42°
Antenna Incidence Angle	48°
Antenna Gain	53.6 dB
Rotation Rate	18.3 rpm
System Loss	7 dB
System Temperature	290 K

3.2.2. PRF Optimization

For the Ka-band DopScat, the PRF optimization processing is the same as that for the Ku-band presented in Section 3.1.2. The simulation results are shown in Figure 19. Here, we list the results of the current field effective swaths with different current velocity Stds in Table 9. The current field effective swaths with different values of PRF are shown in Table 10.

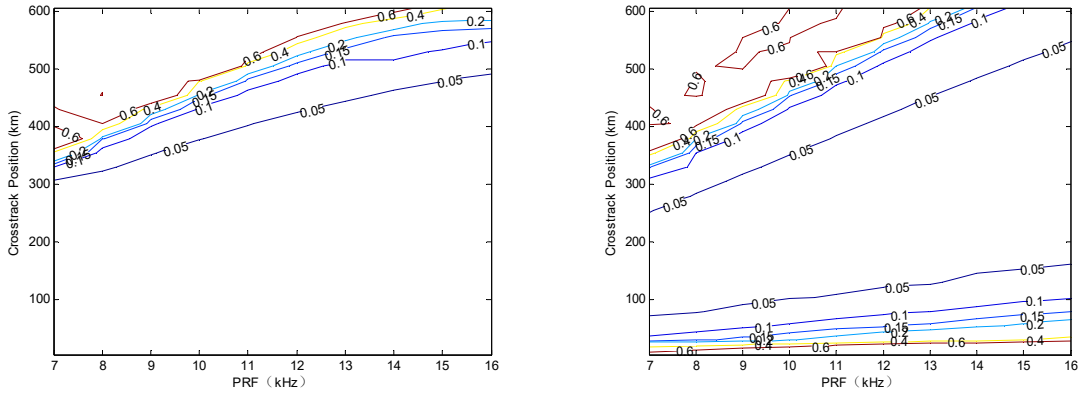

Figure 19. Current velocity components Std with PRF for a wind speed of 7 m/s and a wind direction of 90°: (**a**) along-track direction; (**b**) cross-track direction.

Table 9. Current field effective swaths of different current velocity Stds with different values of PRF.

PRF (kHz)/Current velocity Std (m/s)	7.0	8.0	9.0	10.0	11.0	12.0	13.0	14.0	15.0	16.0
0.05	358	414	452	500	550	592	636	642	650	660
0.10	550	618	682	748	790	854	872	858	874	894
0.15	602	678	750	812	866	914	954	982	986	982
0.20	616	704	782	856	908	960	1004	1034	1048	1040

As shown in Table 9, the current velocity Std could be as small as 0.05 m/s in the Ka-band DopScat, and for a current velocity Std, the effective swath increases as the PRF increases. For example, when the PRF is 8.0 kHz, 10.0 kHz, 12.0 kHz, and 16.0 kHz, the corresponding effective swaths (current

velocity Std of 0.05 m/s) are 414 km, 500 km, 592 km, and 660 km, respectively. Compared with Table 3, we found that the Ka-band could achieve a higher PRF, a smaller current velocity Std, and a larger effective swath than the Ku-band. For example, when the PRF is 10 kHz, the current effective swath (current velocity Std of 0.05 m/s) is 500 km in the Ka-band, while it is impossible to achieve a current velocity Std of 0.05 m/s in the Ku-band. In addition, when the PRF is 10 kHz, the effective swath (current velocity Std of 0.10 m/s) is 748 km in the Ka-band; however, the corresponding effective swath is 358 km in the Ku-band. The Ka-band DopScat could achieve wider-swath and higher-accuracy current measurements than those of in the Ku-band DopScat.

Here, considering the trade-off between current velocity Std and current field effective swath, we choose 0.05 m/s as the current velocity Std to optimize PRF in the Ka-band. The current field effective swaths with different PRF, for current velocity Std of 0.05 m/s, are shown in Table 10.

Table 10. Current field effective swaths (current velocity Std of 0.05 m/s) with different values of PRF.

PRF (kHz)	Duty Cycle	Current Field Effective Swath (km)
7.0	39.81%	358
8.0	38.36%	414
9.0	36.90%	452
10.0	35.45%	500
11.0	34.00%	550
12.0	32.54%	592
13.0	31.09%	636
14.0	29.63%	640
15.0	28.18%	650
16.0	26.72%	660

Figure 19 shows that the current field effective swath increases as the PRF increases. In addition, from Table 10, it is clear that the current field effective swath reaches a maximum of 660 km when the PRF is 16 kHz. Finally, we chose 16 kHz as the optimized PRF.

3.2.3. Bandwidth Optimization

For the Ka-band DopScat, the bandwidth optimization processing is the same as that for the Ku-band presented in Section 3.1.3. We simulated the surface current velocity components Std in the along-track and cross-track directions, and the results are shown in Figure 20. In Table 11, we list the current field effective swaths (current velocity Std of 0.05 m/s) with different bandwidths. Here, we define the effective swath as the cross-track distance, where the current velocity Stds are smaller than 0.05 m/s in both the along-track and cross-track directions.

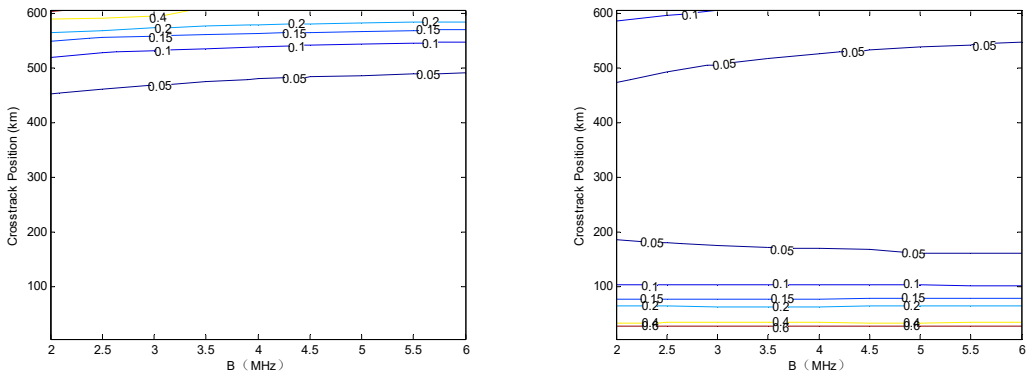

(**a**) (**b**)

Figure 20. Surface current velocity components Std with bandwidths for a wind speed of 7 m/s and a wind direction of 90°: (**a**) along-track direction; (**b**) cross-track direction.

Table 11. Current field effective swaths (current velocity Std of 0.05 m/s) with different bandwidths.

Bandwidth (MHz)	Current Field Effective Swath (km)
2.0	532
2.5	562
3.0	586
3.5	608
4.0	622
4.5	630
5.0	650
5.5	654
6.0	660

The current field effective swath increases as the bandwidth increases. When the bandwidth is 6 MHz, the current field effective swath is the largest, as presented in Table 11. Therefore, we chose 6 MHz as the optimized bandwidth.

3.2.4. System Performance

We simulated the system performance using the system parameters under different wind speed conditions. The results are shown in Figure 21, where σ_V, σ_{Vy}, and σ_{Vx} denote the line-of–sight direction, the cross-track direction, and the along-track direction.

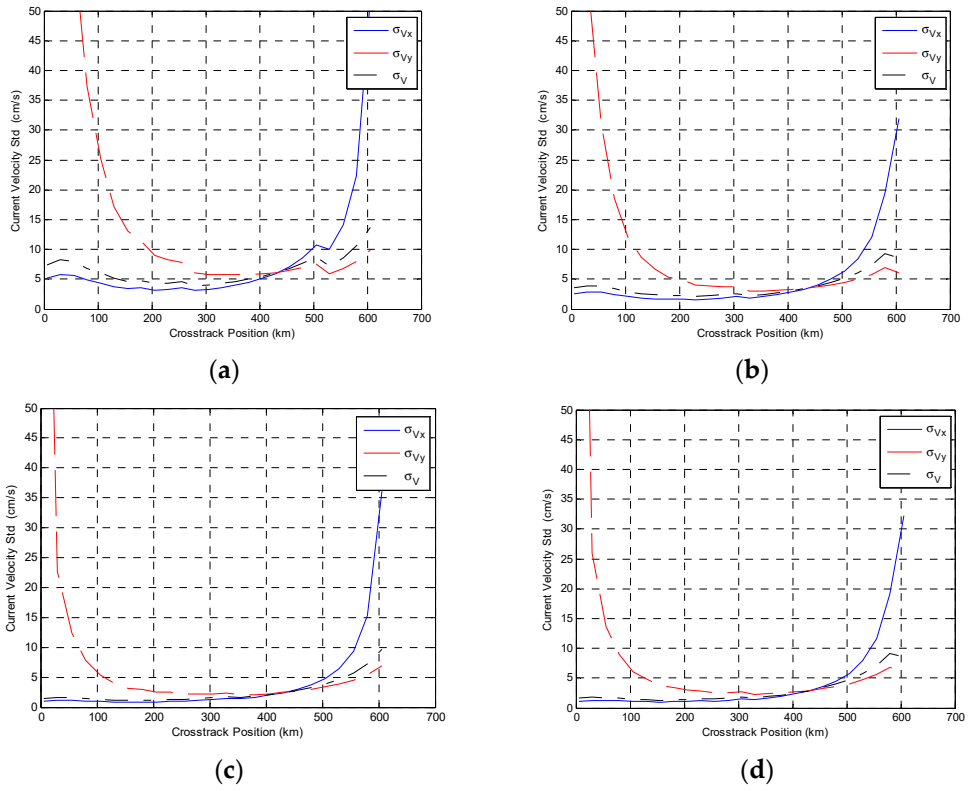

Figure 21. Surface current velocity components Std in line-of-sight, cross-track, and along-track direction: (**a**) U = 4 m/s; (**b**) U = 7 m/s; (**c**) U = 14 m/s; (**d**) U = 21 m/s.

Overall, the current field effective swath is small in low wind speeds, but it has good performance in high wind speeds, as shown in Figure 21. In order to analyze the current field effective swaths of different current velocity Stds with different wind speeds more directly, we examined Table 12.

Table 12. Current field effective swaths of different current velocity Stds in different wind speeds.

Wind Speed (m/s)/Current Velocity Std (m/s)	2	3	4	5	6	7	8	9	12	15	18
0.05	-	-	-	376	560	660	706	738	784	790	766
0.10	-	272	602	758	842	894	920	944	976	982	990
0.15	-	640	830	896	942	982	1006	1028	1058	1060	1048
0.20	468	750	904	978	1008	1038	1068	1080	1096	1100	1107

As shown in Table 12, the Ka-band DopScat could achieve wide-swath and high-accuracy current measurements. When the wind speeds are 6 m/s, 7 m/s, 8 m/s, 9 m/s, 12 m/s, 15 m/s, and 18 m/s, the corresponding current effective swaths (for a current velocity Std of 0.05 m/s) are 560 km, 660 km, 706 km, 738 km, 784 km, 790 km, and 766 km, respectively. This indicates that the Ka-band DopScat could achieve wider-swath and higher-accuracy current measurements.

4. Effects of Satellite Attitude and Velocity Determinations on Current Retrieval

From Equations (17) and (18) in Section 2.4, current velocity components V_x and V_y are related to the incidence angle, observation azimuth, and satellite velocity, and in turn, the incidence, observation azimuth, and satellite velocity determination affect the current velocity accuracy. The measurement errors of incidence angle and observation azimuth are caused by satellite attitude determinations, where satellite attitude contains the pitch, the yaw, and the roll.

4.1. Effects of Satellite Attitude Determinations on Incidence Angle and Observation Azimuth

The variation of incidence angle and observation azimuth errors caused by the pitch, the yaw, and the roll in different observation azimuths are shown in Figure 22. As for the satellite attitude determinations, the star sensor adopts three warm backups using archive-log mode. A satellite attitude determination of 0.001° is achievable in the post-processing by multi-sensor fusion, combining the three warm backup data with high accuracy optical encoder data. Therefore, the pitch, the yaw, and the roll determination of 0.001° is feasible in post-processing.

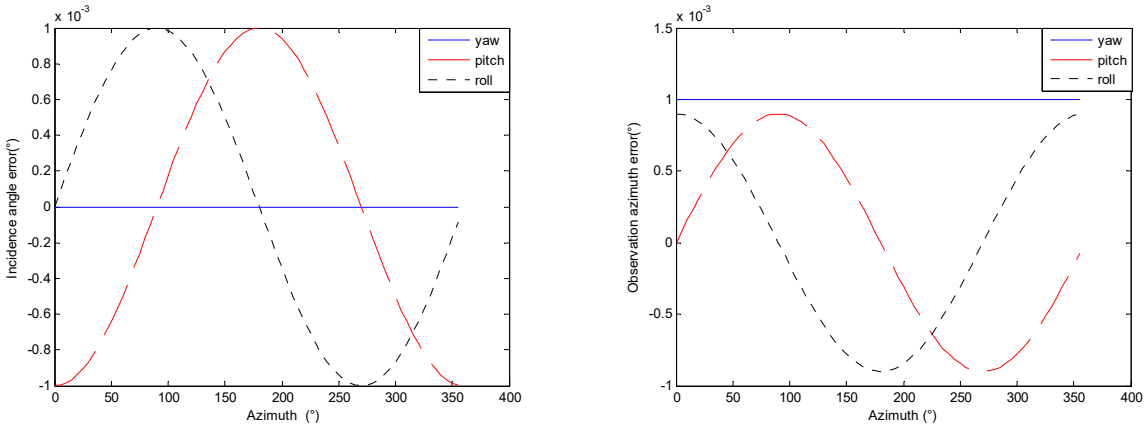

Figure 22. Incidence angle and observation azimuth measurement errors caused by satellite attitude determinations: (**a**) incidence angle error; (**b**) observation azimuth error.

As shown in Figure 22a, the yaw determination has no effect on incidence angle error, the roll effect on incidence angle error is largest when the azimuth is 90° (i.e., side-looking), and the pitch effect on incidence angle error is largest when the azimuth is 0° (i.e., forward-looking) or 180° (i.e., afterward-looking). In Figure 22b, the yaw effect on observation azimuth error is a constant;

it does not vary with azimuths. The roll effect on incidence angle error reaches a maximum when the azimuth is 0°or 180°, and the pitch on incidence angle error reaches a maximum when the azimuth is 90°.

4.2. Effects of Satellite Attitude and Velocity Determinations on Current Retrieval

The satellite attitude and velocity determinations effects on current retrieval are shown in Figure 23, where velocity error unit is cm/s.

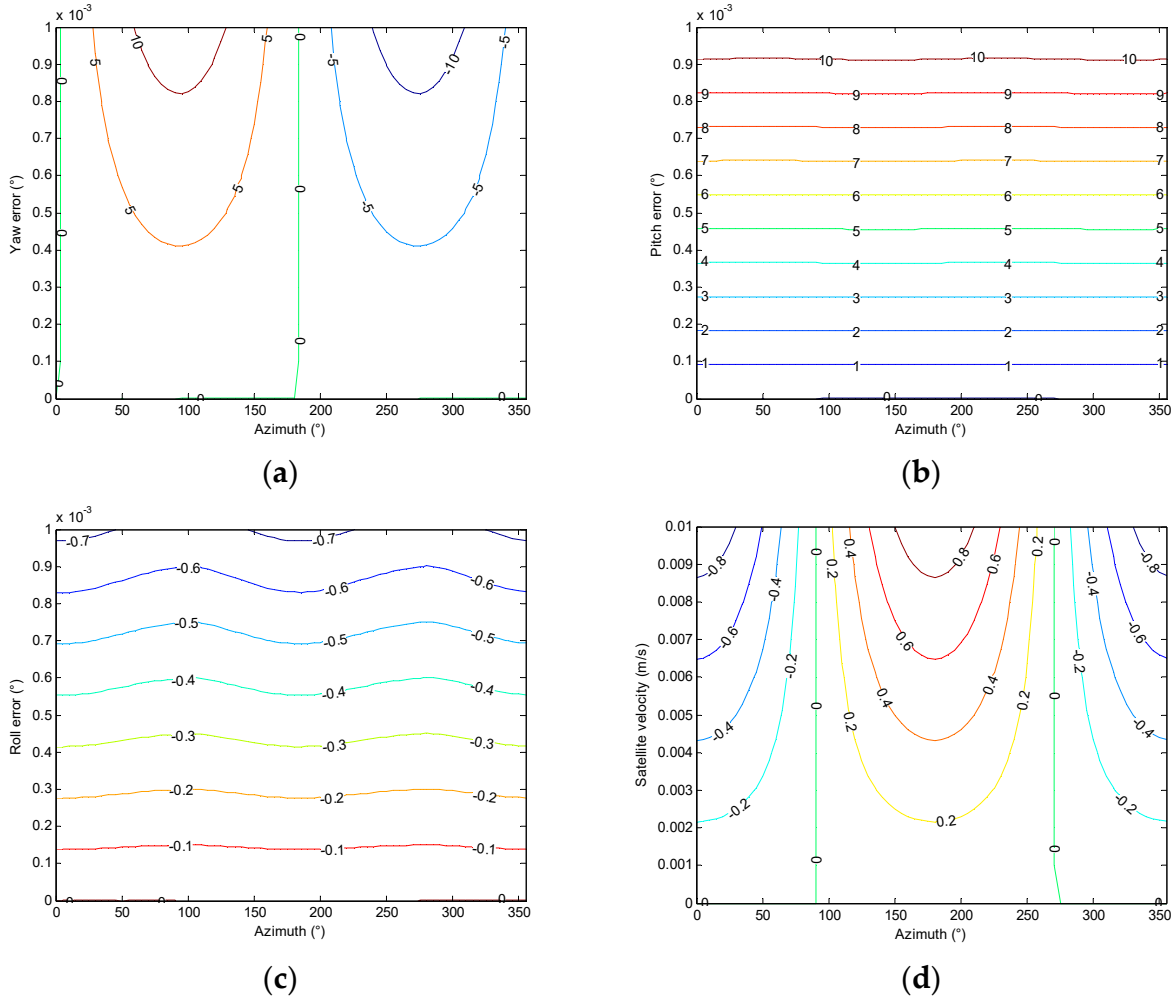

Figure 23. Satellite attitude and velocity determinations effects on current retrieval: (**a**) yaw; (**b**) pitch; (**c**) roll; (**d**) satellite velocity.

In Figure 23, we found that the effects of roll and satellite velocity determinations on current retrieval are smaller than those of the yaw and the pitch. When the roll determination is smaller than 0.001°, the current velocity error is less than 0.7 cm/s. Also, the current velocity error is less than 0.8 cm/s when the satellite velocity determination is smaller than 0.01 m/s.

The yaw, pitch, roll, and satellite velocity determinations are mutually independent random variables, so current velocity errors caused by satellite attitude and velocity determinations can be expressed as:

$$\Delta V = \sqrt{\Delta V_{yaw}^2 + \Delta V_{pitch}^2 + \Delta V_{roll}^2 + \Delta V_{V_{sat}}^2}. \quad (26)$$

Here ΔV_{yaw}, ΔV_{pitch}, ΔV_{roll}, and $\Delta V_{V_{sat}}$ denote yaw, pitch, roll, and satellite velocity determination, respectively. The effects of these determinations on ocean current velocity error are shown in Figure 24.

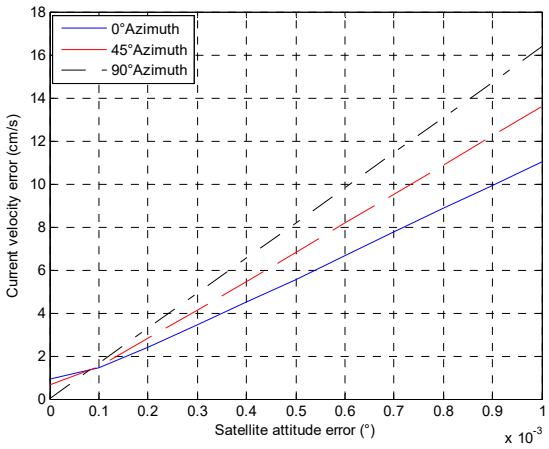

Figure 24. Effects of satellite attitude and velocity determinations on current velocity error.

As shown in Figure 24, the current velocity error increases linearly with satellite attitude determinations. When the observation azimuth is 90°, the effect of satellite attitude and velocity determinations on current velocity error is largest, around 16.37 cm/s.

5. Conclusions

Wind speed and direction errors have a non-negligible effect on current retrieval. Ocean surface current velocity error is sensitive to wind speed and direction errors. For HH polarization, the current velocity error could be as large as 0.25 m/s for a wind speed error of 2 m/s, while it gets even smaller than 0.50 m/s in case of a wind direction error that is smaller than 20° in the crosswind direction. In the case of VV polarization, the ocean surface current velocity error could be as large as 0.14 m/s for a wind speed error of 2 m/s, and could reach values smaller than 0.40 m/s for wind direction errors smaller than 20° in the crosswind direction. So, it is necessary to obtain real-time wind field information to mitigate the wind effects on current retrieval. This is why we proposed a Ku-Ka dual-frequency scatterometer, keeping the Ku-band mainly for wind measurement and keeping the Ka-band for current measurement.

We established an end-to-end dual-frequency DopScat system simulation model and simulated the system performance in Section 3. The results indicate that the Ku-band DopScat could be a feasible method to measure ocean surface current, but with low accuracy and a small current field effective swath. Comparing the K_{pc} of the Ku-band DopScat with that of the HY-2A scatterometer, it is indicated that the wind performance of the Ku-band DopScat is better than that of the HY-2A scatterometer (where wind speed accuracy is 2 m/s, the wind direction accuracy is 20°). Our results indicate that the Ku-band DopScat could provide more accurate wind field information than the HY-2A scatterometer.

In the simulation of the Ka-band DopScat, we chose 6 MHz as transmit signal bandwidth and 16 kHz as the PRF. The results show that the current velocity Std could be smaller than 0.05 m/s when the wind speed is larger than 5 m/s. The Ka-band DopScat also has a better performance in the condition of low wind speed, e.g., when the wind speed is larger than 2 m/s, the current velocity Std would be smaller than 0.10 m/s. When the wind speed is 7m/s, for current velocity Stds of 0.05 m/s, 0.10 m/s, and 0.15 m/s, and the corresponding current field effective swaths are 660 km, 894 km, and 982 km, respectively. This indicates that the Ka-band DopScat can achieve wide-swath and high-accuracy current measurements.

In addition, we discussed the satellite attitude and velocity determinations effects on ocean current retrieval in Section 4, and the results show that the effect of satellite attitude and velocity determinations on current velocity error would be 16.37 cm/s when in the side-looking direction.

Our results indicate that a Ku-Ka dual-frequency DopScat could be a feasible method for wide-swath and high-accuracy simultaneous measurements of ocean surface wind and current.

Author Contributions: Y.M. and X.D. proposed and simulated the system design; Q.B. established the correlation model in the system simulation; Y.M. performed the system simulation; Y.M. and X.D. analyzed the system simulation results; Y.M. and X.D. wrote the manuscript; D.Z. edited the manuscript.

Funding: The work of this paper is partly supported by National Key Research and Development Program of China (Contract No. 2016YFC1401002).

Conflicts of Interest: The authors declare no conflict of interest.

References

1. Kelly, K.A.; Dickinson, S.; Mcphaden, M.J.; Johnson, C.C. Ocean currents evident in satellite wind data. *Geophys. Res. Lett.* **2001**, *28*, 2469–2472. [CrossRef]
2. Chelton, D.B.; Schlax, M.G.; Freilich, M.H.; Milliff, R.F. Satellite measurements reveal persistent small-scale features in ocean winds. *Science* **2004**, *303*, 978–983. [CrossRef] [PubMed]
3. Drever, R.G.; Sanford, T. *A Free-Fall Electromagnetic Current Meter Instrumentation*; Woods Hole Oceanographic Institution: Woods Hole, MA, USA, 1971; pp. 353–370.
4. Brumley, B.H.; Cabrera, R.G.; Deines, K.L.; Terray, E.A. Performance of a broad-band acoustic Doppler current profiler. *IEEE J. Ocean. Eng.* **1991**, *16*, 402–407. [CrossRef]
5. Gong, Z.; Ke, H.; Hou, J.; Wu, X.; Cheng, F. Error analyze of current measurements by HF surface wave radar. *J. Wuhan Univ. Nat. Sci. Ed.* **2007**, *53*, 356–360.
6. Bernstein, R.L.; Born, G.H.; Whritner, R.H. SEASAT altimeter determination of ocean current variability. *J. Geophys. Res. Oceans* **1982**, *87*, 3261–3268. [CrossRef]
7. Romeiser, R.; Johannessen, J.; Chapron, B.; Collard, F.; Kudryavtsev, V.; Runge, H.; Suchandt, S. *Direct Surface Current Field Imaging from Space by Along-Track InSAR and Conventional SAR*; Oceanography from Space; Springer: Dordrecht, The Netherlands, 2010; pp. 73–91.
8. Chapron, B.; Collard, F.; Ardhuin, F. Direct measurements of ocean surface velocity from space: Interpretation and validation. *J. Geophys. Res. Oceans* **2005**, *110*, 691–706. [CrossRef]
9. Fabry, P.; Recchia, A.; de Kloe, J.; Stoffelen, A.; Husson, R.; Collard, F.; Chapron, B.; Mouche, A.; Enjolras, V.; Johannessen, J.; et al. *Feasibility Study of Sea Surface Currents Measurements with Doppler Scatterometers*; ESA Living Planet Programme, 16/9/2013–20/9/2013; ESA: Edinburgh, UK, 2013.
10. Stoffelen, A.; de Kloe, J.; Johannessen, J.; Mouche, A.; Collard, F.; Chapron, B.; Enjolras, V.; Recchia, A.; D'Aria, D.; Fois, F.; et al. Feasibility Assessment of Simultaneous Ocean Wind and Current Measurements. In Proceedings of the International Ocean Vector Wind Science Team Meeting, Annapolis, Maryland, USA, 9–11 May 2011.
11. Rodriguez, E. Wide Swath Simultaneous Measurements of Winds and Surface Currents. In Proceedings of the International Ocean Vector Wind Science Team Meeting, Utrecht, The Netherlands, 12–14 June 2012.
12. Rodriguez, E.; Perkovic-Martin, D.; Baldi, C.; Cooper, K.; Majurec, N.; Neumann, M.; Nicaise, F.; Farquharson, G. Ka-band Doppler scatterometer for measurements of ocean surface vector winds and currents. In Proceedings of the Earth Science Technology Forum, Leesburg, Virginia, USA, 8–30 October 2014.
13. Fois, F.; Hoogeboom, P.; Chevalier, F.L.; Stoffelen, A. DOPSCAT: A mission concept for a Doppler wind-scatterometer. In Proceedings of the 2015 IEEE International Geoscience and Remote Sensing Symposium (IGARSS), Milan, Italy, 26–31 July 2015; pp. 2572–2575.
14. Fois, F.; Hoogeboom, P.; Chevalier, F.L.; Stoffelen, A.; Mouche, A. DopSCAT: A mission concept for simultaneous measurements of marine winds and surface currents. *J. Geophys. Res. Oceans* **2015**, *120*, 7857–7879. [CrossRef]
15. Bao, Q.; Dong, X.; Zhu, D.; Lang, S.; Xu, X. The feasibility of ocean surface current measurement using pencil-beam rotating scatterometer. *IEEE J. Sel. Top. Appl. Earth Obs. Remote Sens.* **2015**, *8*, 3441–3451. [CrossRef]
16. Romeiser, R.; Thompson, D.R. Numerical study on the along-track interferometric radar imaging mechanism of oceanic surface currents. *IEEE Trans. Geosci. Remote Sens.* **2000**, *38*, 446–458. [CrossRef]
17. Romeiser, R.; Alpers, W.; Wismann, V. An improved composite surface model for the radar backscattering cross section of the ocean surface: 1. Theory of the model and optimization/validation by scatterometer data. *J. Geophys. Res. Oceans* **1997**, *102*, 25237–25250. [CrossRef]

18. Apel, J.R. An improved model of the ocean surface wave vector spectrum and its effects on radar backscatter. *J. Geophys. Res. Oceans* **1994**, *99*, 16269–16291. [CrossRef]
19. Longuet-Higgins, M.S.; Cartwright, D.E.; Smith, N.D. Observations of the directional spectrum of sea waves using the motions of a floating buoy. In *Ocean Wave Spectrum*; Prentice Hall: Upper Saddle River, NJ, USA, 1963; pp. 111–136.
20. Yurovsky, Y.; Kudryavtsev, V.N.; Chapron, B.; Grodsky, S.A. Modulation of Ka-Band Doppler Radar Signals Backscattered from the Sea Surface. *IEEE Trans. Geosci. Remote Sens.* **2018**, *56*, 2931–2948. [CrossRef]
21. Rodríguez, E.; Wineteer, A.; Perkovic-Martin, D.; Gál, T.; Stiles, B.W.; Niamsuwan, N.; Monje, R.R. Estimating Ocean Vector Winds and Currents Using a Ka-Band Pencil-Beam Doppler Scatterometer. *Remote Sens.* **2018**, *10*, 576. [CrossRef]
22. Wentz, F.J.; Freilich, M.H.; Smith, D.K. NSCAT-2geophysical model function. In Proceedings of the Fall AGU Meeting, San Francisco, CA, USA, 6–10 December 1998; pp. 1–10.
23. Bao, Q. System Design and Simulation of Doppler Scatterometer—Wide Swath Ocean Surface Current Measurement. Ph.D. Thesis, University of Chinese Academy of Sciences, Beijing, China, 2015.
24. Spencer, M.W. A Methodology for the Design of Spaceborne Pencil-Beam Scatterometer Systems. Ph.D. Thesis, Brigham Young University, Provo, UT, USA, 2001.